ARMA 14-6959

Using Microstructure Descriptors to Model Thermo-mechanical Damage and Healing in Salt Rock

Zhu, C. and Arson, C.
Geosystems group, School of Civil and Environmental Engineering,
Georgia Institute of Technology, Atlanta, Georgia, USA.

ABSTRACT: Creep processes in halite (salt rock) include glide, cross-slip, diffusion and dynamic recrystallization. Diffusive Mass Transfer (DMT) can result in crack rebonding, and mechanical stiffness recovery. On the one hand, viscoplastic laws relating creep microscopic processes to microstructure changes are empirical. On the other hand, theoretical models of damage and healing disconnect thermodynamic variables from their physical meaning. The proposed model enriches the framework of Continuum Damage Mechanics (CDM) with fabric descriptors. In order to infer the form of fabric tensors from microstructure observation, creep tests were carried out on granular salt under constant stress and humidity conditions. A stress path comprising a tensile loading, a compressive unloading, a creep-healing stage and a reloading was simulated. Macroscopic and microscopic model predictions highlight the increased efficiency of healing with time. A preliminary Finite Element model illustrates the impact of healing on the stress distribution in the Excavation Damage Zone (EDZ). The model presented in this paper is expected to improve the fundamental understanding of damage and healing in rocks at both macroscopic and microscopic levels, and the long-term assessment of geological storage facilities.

1. INTRODUCTION

Geotechnical reservoirs and repositories in rocks such as nuclear waste disposals, geothermal systems, and compressed gas storage are usually subjected to high stress and temperature gradients. Salt rock is an attractive choice for host rock because of its favorable creep characteristics and low gas permeability. Design and long-term assessment of those facilities using salt rock require a better understanding of damage and healing mechanisms.

Most damage and healing thermo-mechanical models proposed for salt rock are based on the concept of dilatancy boundary. Anisotropic healing models based on Continuum Damage Mechanics (CDM) usually resort to the concept of "net damage", which allows modeling stiffness decrease (damage) and increase (healing). These theoretical frameworks are usually purely hypothetical and do not allow the prediction of actual rock materials. Moreover, existing rock damage models distinguishing closure and rebonding conveniently resort to rate-dependent evolution laws for all dissipation variables, which avoids the challenges associated to the requirement on the positivity of dissipation. However, such models do not properly represent the evolution of brittle behavior associated to rate-independent crack opening and closure, and actually consider healing as a particular form of crack closure (detected by an increase of wave velocity) rather than crack rebonding.

The goal of this study is to enrich a continuum thermo-mechanical framework of anisotropic damage and Diffusive Mass Transfer (DMT)-induced crack rebonding with fabric descriptors. There are two types of self-healing systems recognized so far, including active system triggered by damage mechanisms, and passive system requiring external simulation. The damage and healing model proposed in this paper belongs to the category of uncoupled passive system, analogous to the close-then-heal scheme [1].

Section 2 presents a study of fabric descriptors based on image analysis performed during creep tests of granular table salt. The multi-scale theoretical framework coupling crack opening, closure and healing is explained in Section 3. Section 4 presents a preliminary Finite Element analysis performed in elasticity to study the impact of healing in the Excavation Damage Zone (EDZ).

2. MICROSTRUCTURE CHARACTERIZATION

2.1. Experimental Study of Creep in Table Salt

In practice, it is challenging to observe the damage propagation associated with microstructure evolution in salt rock during a loading test. Table salt has the same crystallographic structure and halite content as salt rock. Therefore, it can be used to simulate the creep process occurred in salt rock. In the experiment described below, salt grains were confined in tubes with both ends fixed by nails. The tubes were placed in a chamber with controlled moisture conditions, at room temperature (Fig. 1). Constant humidity was ensured by adding saturated salt water to the bottom of the container, as explained in [2]. Constant load was applied through the compression of the springs with the same rigidity. Three different initial spring elongations were chosen in order to apply three specific pressures: 0.1MPa, 0.15MPa, and 0.2MPa. Constant stress could be maintained since the deformed spring length was almost unchanged throughout the test.

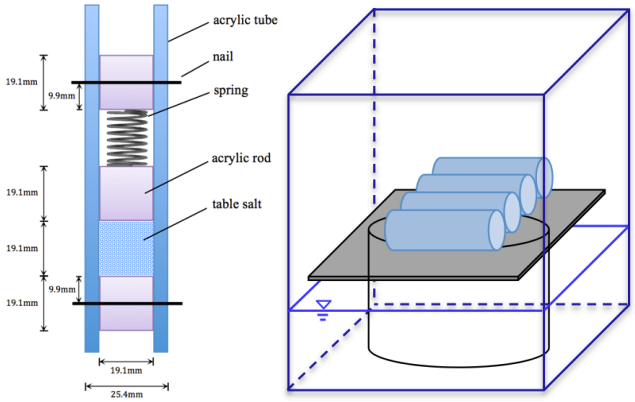

Fig. 1. Experimental set-up for the creep test performed on table salt.

2.2. Image Analysis

Microscopic images of salt were recorded at regular time intervals. Transparent salt particles reflect light at their planar surfaces during the stereoscopic observation, which impairs quality of the image. ImageJ application [3] was used for image processing. Figure 2 presents the principle of the image analysis. After enhancing the contrast and removing the background, a binary image was obtained. Removing outliers and filtering steps helped achieving an image of better quality. The black regions indicate the presence of void space between salt grains. Fabric analysis was then carried out to determine appropriate fabric descriptors.

Through testing of several shapes, fitting ellipses presented the best match with void contours. Statistical results indicated that the probability density function of ellipses' area ("Void area", A_v) follows a power law distribution:

$$p_A(A_v) = a \cdot A_v^t \quad (1)$$

Fitting of microscopic data provided: $a = 5{\times}10^{-5}$ and $t = -1.2$. Despite the existence of several spikes, the projections of the major semi-axes in three principal directions of space (noted as crack length R_i) were found to follow a lognormal distribution:

$$p_i(R_i) = \frac{1}{\sqrt{2\pi}R_i s_i} e^{-\frac{(lnR_i - m_i)^2}{2s_i^2}} \quad (2)$$

In which s_i is the standard deviation and m_i is the mean value.

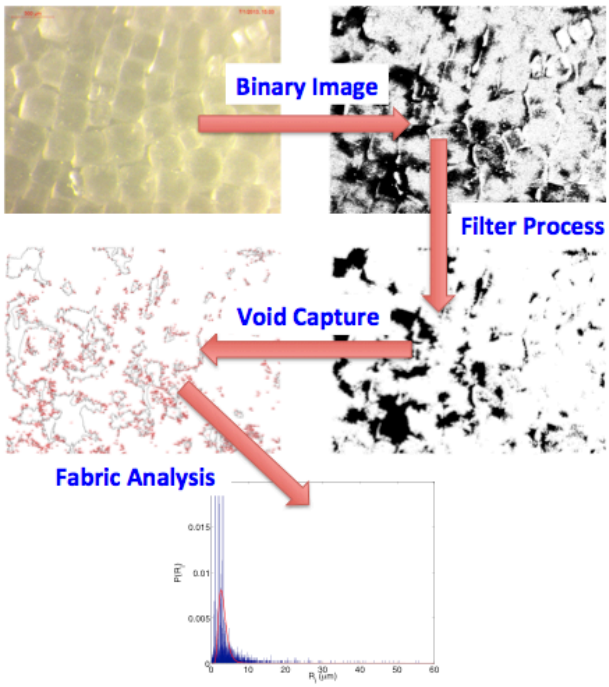

Fig. 2. Principle of the image analysis.

3. THEORETICAL FRAMEWORK

The proposed model in this paper couples microscopic and macroscopic thermo-mechanical evolution laws, in order to capture the effects of micro-crack on deformation and stiffness. Table 1 summarizes the outline of the Continuum Damage Mechanics (CDM) model used as a basis to study Diffusive Mass Transfer (DMT)-induced healing [4].

3.1. Continuum Damage Model

For a typical loading-unloading cycle, total deformation can be decomposed into three components (Fig. 3). $\boldsymbol{\varepsilon^{el}}$ is the purely elastic deformation and is recoverable upon unloading. $\boldsymbol{\varepsilon^{d}}$ denotes the damage deformation induced by crack propagation and has two components: $\boldsymbol{\varepsilon^{ed}}$ is the damage-induced elastic deformation, $\boldsymbol{\varepsilon^{id}}$ is the irreversible deformation due to residual crack openings.

The summation of $\boldsymbol{\varepsilon^{el}}$ and $\boldsymbol{\varepsilon^{ed}}$ gives the total elastic deformation $\boldsymbol{\varepsilon^{E}}$. The additional compression stress required to compensate $\boldsymbol{\varepsilon^{id}}$ is referred to as the residual stress:

$$\boldsymbol{\sigma_R = -D(\Omega)}:\boldsymbol{\varepsilon^{id}} \tag{3}$$

In which $\boldsymbol{D}$ is the stiffness tensor, $\boldsymbol{D_0}$ indicates the stiffness at undamaged state. $\boldsymbol{\Omega}$ is the damage variable.

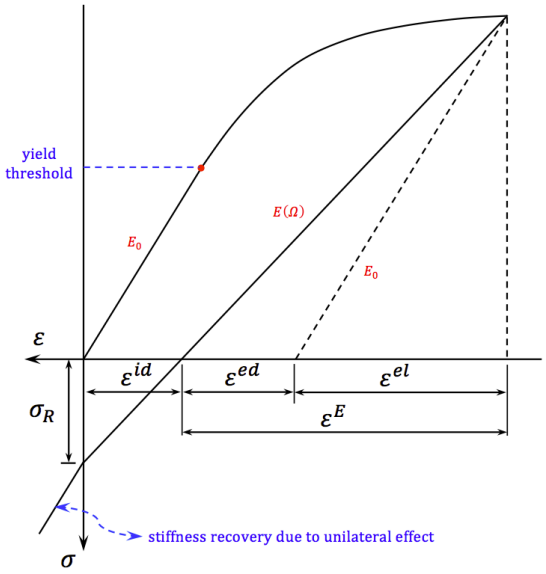

Fig. 3. Decomposition of deformation (soil mechanics sign convention: compression counted positive)

The solid skeleton free energy consists of the purely thermo-elastic deformation energy (ψ_s^{ET}) and the potential energy of crack faces ($\psi_s^{\Omega T}$).

Thermodynamic conjugation relationships give the stress and the damage driving force [5]. A dimensional analysis shows that the quadratic term in temperature $\frac{\tau^2}{2\tau_0}\frac{\partial C(\boldsymbol{\Omega})}{\partial \boldsymbol{\Omega}}$ is negligible. For simplicity, the damage criterion is independent of temperature variation. The active damage driving force ($\boldsymbol{Y_d}$) is further simplified as a function of total strain only.

To capture the hardening phenomenon, which accounts for the release of energy needed for growth of micro-cracks, the damage criterion is expressed in the form of a norm minus the damage threshold (Table 1).

Following a classical CDM assumption [6], the damage flow rule is assumed to be associative, i.e., f_d is used as the damage potential:

$$d\boldsymbol{\Omega} = d\lambda_d \frac{\partial f_d(\boldsymbol{Y_d}, \boldsymbol{\Omega})}{\partial \boldsymbol{Y_d}} = \frac{[\frac{\boldsymbol{Y_d}}{\sqrt{2\boldsymbol{Y_d}:\boldsymbol{Y_d}}}]:d\boldsymbol{Y_d}}{(C_1\boldsymbol{\delta}):[\frac{\boldsymbol{Y_d}}{\sqrt{2\boldsymbol{Y_d}:\boldsymbol{Y_d}}}]}:[\frac{\boldsymbol{Y_d}}{\sqrt{2\boldsymbol{Y_d}:\boldsymbol{Y_d}}}] \tag{4}$$

Cracks are considered as closed when their faces are in contact but not bonded. Crack closure is accounted for by adapting the concept of unilateral effect, which refers to the recovery of material compressive strength due to closure of tensile cracks.

Following Chaboche's approach [7], stiffness depends on a Heaviside function to distinguish the behaviors in tension and compression. Crack closure increases the number of inter-granular contacts in the Representative Element Volume (REV), which results in a recovery of stiffness ($\boldsymbol{D}^*(\boldsymbol{\Omega})$) as well as heat capacity ($C^*(\boldsymbol{\Omega})$).

3.2. Diffusive Mass Transfer-induced Healing

In the proposed model, healing does not occur upon bare crack closure. An energy input is required to trigger the migration of ions within the lattice, and is therefore a dissipative process independent from damage [8]. Diffusive Mass Transfer (DMT) is the main driving factor for crack rebonding at low temperature. Cracks tend to be sealed by different ionic species at the crack faces. The intra-granular diffusion is assumed to be an isotropic phenomenon because of the uniform distribution of grain orientations. The healing tensor reduces to a scalar: $\boldsymbol{H} = h\boldsymbol{\delta}$. Damage is considered as a rate-independent dissipation variable in the proposed model. The consistency equation impose that damage cannot decrease. A mixed damage variable $\boldsymbol{A}$ is introduced (Table 1), which represents the difference between damage and healing. Therefore, the expressions of the recovered stiffness and heat capacity depend on $\boldsymbol{A}$ instead of $\boldsymbol{\Omega}$.

A diffusion equation is used to model the migration of sodium ions from salt grain bulk to its boundaries. The intensity of net damage, defined as $u = U_0 - h$, satisfies the diffusion equation:

$$\frac{\partial u}{\partial t} = D_c \nabla^2 u \tag{5}$$

In which D_c is the diffusion coefficient and U_0 is the intensity of damage in the REV before healing occurs:

$$U_0 = tr(\Omega)_{t=0} \tag{6}$$

Half of the edge length of the grain is taken as the maximum diffusion distance. Crack healing is considered as complete when an ion reaches a crack face and electronic forces bonds this ion to the lattice of the opposite crack face. At the boundaries, the net damage is taken as zero. The initial conditions for healing in the REV are:

$$h(x, t=0) = 0, \quad u(x, t=0) = U_0 \tag{7}$$

Therefore, the solution writes:

$$u(x,t) = \frac{4U_0}{\pi} \sum_{i=1,3,5,\dots}^{\infty} \frac{e^{-\lambda_n^2 D_c t} \sin(\lambda_n x)}{n} \tag{8}$$

In which $\lambda_n = \frac{n\pi}{l}$.

Table 1. Outline of thermo-mechanical damage and healing model

Postulates	
Free Energy for Crack Opening (Ψ_S)	$\psi_s = \psi_s^{ET} + \psi_s^{\Omega T} = \left[\frac{1}{2}\boldsymbol{\varepsilon^{el}}\colon\boldsymbol{D_0}\colon\boldsymbol{\varepsilon^{el}} - \frac{C_0\tau^2}{2\tau_0} - \tau\boldsymbol{K_0}\colon\boldsymbol{\varepsilon^{el}}\right] + [\frac{1}{2}\boldsymbol{\varepsilon^{d}}\colon\boldsymbol{D}(\boldsymbol{\Omega})\colon\boldsymbol{\varepsilon^{d}} - \frac{C(\boldsymbol{\Omega})\tau^2}{2\tau_0} - \tau\boldsymbol{K}(\boldsymbol{\Omega})\colon\boldsymbol{\varepsilon^{d}}]$ $\frac{1}{2}\boldsymbol{\varepsilon^{d}}\colon\boldsymbol{D}(\boldsymbol{\Omega})\colon\boldsymbol{\varepsilon^{d}} = \frac{1}{2}\lambda\left(tr\boldsymbol{\varepsilon^{d}}\right)^2 + \mu tr\left(\boldsymbol{\varepsilon^{d}}\cdot\boldsymbol{\varepsilon^{d}}\right) + \alpha tr\boldsymbol{\varepsilon^{d}} tr\left(\boldsymbol{\varepsilon^{d}}\cdot\boldsymbol{\Omega}\right) + 2\beta tr(\boldsymbol{\varepsilon^{d}}\cdot\boldsymbol{\varepsilon^{d}}\cdot\boldsymbol{\Omega})$
Free Energy for Crack Closure (Ψ_S)	$\psi_s = \left[\frac{1}{2}\boldsymbol{\varepsilon^{el}}\colon\boldsymbol{D_0}\colon\boldsymbol{\varepsilon^{el}} - \frac{C_0\tau^2}{2\tau_0} - \tau\boldsymbol{K_0}\colon\boldsymbol{\varepsilon^{el}}\right] + [\frac{1}{2}\boldsymbol{\varepsilon^{d}}\colon\boldsymbol{D^*}(\boldsymbol{\Omega})\colon\boldsymbol{\varepsilon^{d}} - \frac{C^*(\boldsymbol{\Omega})\tau^2}{2\tau_0} - \tau\boldsymbol{K^*}(\boldsymbol{\Omega})\colon\boldsymbol{\varepsilon^{d}}]$ $\boldsymbol{D^*}(\boldsymbol{\Omega}) = \boldsymbol{D}(\boldsymbol{\Omega}) + \eta\sum_{i=1}^{3} H\left(-tr(\boldsymbol{P}_i\colon\boldsymbol{\varepsilon})\right)\boldsymbol{P}_i\colon\left(\boldsymbol{D_0} - \boldsymbol{D}(\boldsymbol{\Omega})\right)\colon\boldsymbol{P}_i,\ 0<\eta\le 1$ $\boldsymbol{K^*}(\boldsymbol{\Omega}) = \boldsymbol{K}(\boldsymbol{\Omega}) + \eta\sum_{i=1}^{3} H\left(-tr(\boldsymbol{P}_i\colon\boldsymbol{\varepsilon})\right)\boldsymbol{P}_i\colon\left(\boldsymbol{K_0} - \boldsymbol{K}(\boldsymbol{\Omega})\right)\colon\boldsymbol{P}_i,\ 0<\eta\le 1$ $C^*(\boldsymbol{\Omega}) = C(\boldsymbol{\Omega}) + \eta\sum_{i=1}^{3} H\left(-tr(\boldsymbol{P}_i\colon\boldsymbol{\varepsilon})\right)\boldsymbol{P}_i\colon\left[\left(C_0 - C(\boldsymbol{\Omega})\right)\boldsymbol{\delta}\otimes\boldsymbol{\delta}\right]\colon\boldsymbol{P}_i,\ 0<\eta\le 1$
Free Energy for Crack Rebonding (Ψ_S)	Replace $\boldsymbol{\Omega}$ by $\boldsymbol{A}$ in the free energy for crack closure $\boldsymbol{A} = \boldsymbol{\Omega} - \boldsymbol{\delta}h$
Damage Criterion (f_d)	$f_d(\boldsymbol{Y_d}, \boldsymbol{\Omega}) = \sqrt{\frac{1}{2}\boldsymbol{Y_d}\colon\boldsymbol{Y_d}} - [a_0 + a_1\mathrm{tr}(\boldsymbol{\Omega})]$
Strain Decomposition	$\boldsymbol{\varepsilon} = \boldsymbol{\varepsilon^E} + \boldsymbol{\varepsilon^{id}} = \boldsymbol{\varepsilon^{el}} + \boldsymbol{\varepsilon^{d}} = \boldsymbol{\varepsilon^{el}} + \boldsymbol{\varepsilon^{ed}} + \boldsymbol{\varepsilon^{id}}$
Diffusion Equation	$\bar{u}(t) = < u(x,t) > = \frac{1}{l}\int_0^l u(x,t)dx = \frac{8U_0}{\pi l}\sum_{i=1,3,5,\dots}^{\infty}\frac{e^{-\lambda_n^2 D_c t}}{n\lambda_n}$ $D_c = D_{c0}e^{-\frac{Q}{RT}}$ $h(t) = 1 - \bar{u}(t)$
Conjugation relationships	
Stress ($\boldsymbol{\sigma}$)	$\boldsymbol{\sigma} = \frac{\partial\psi_S}{\partial\boldsymbol{\varepsilon^{el}}} = \boldsymbol{D_0}\colon\boldsymbol{\varepsilon^{el}} - \tau\boldsymbol{K_0}$
Damage Driving Force (Y_d)	$\boldsymbol{Y} = -\frac{\partial\psi_S}{\partial\boldsymbol{\Omega}} = -\left[\boldsymbol{D}(\boldsymbol{\Omega})\colon\boldsymbol{\varepsilon^{d}}\right]\colon\frac{\partial\boldsymbol{\varepsilon^{d}}}{\partial\boldsymbol{\Omega}} - \frac{1}{2}\boldsymbol{\varepsilon^{d}}\colon\frac{\partial\boldsymbol{D}(\boldsymbol{\Omega})}{\partial\boldsymbol{\Omega}}\colon\boldsymbol{\varepsilon^{d}} + \frac{\tau^2}{2\tau_0}\frac{\partial C(\boldsymbol{\Omega})}{\partial\boldsymbol{\Omega}} + \tau\boldsymbol{K}(\boldsymbol{\Omega})\colon\frac{\partial\boldsymbol{\varepsilon^{d}}}{\partial\boldsymbol{\Omega}} + \tau\frac{\partial\boldsymbol{K}(\boldsymbol{\Omega})}{\partial\boldsymbol{\Omega}}\colon\boldsymbol{\varepsilon^{d}}$ $\boldsymbol{Y_d} = -(\alpha + 2\beta)\boldsymbol{\varepsilon}\cdot\boldsymbol{\varepsilon}$

α, β	=	mechanical damage parameters	a_0	=	initial damage threshold
λ, μ	=	Lam*é* coefficients	a_1	=	damage hardening parameter
τ_0	=	initial temperature	g	=	toughness parameter
$\boldsymbol{D}$	=	damaged stiffness tensor	k	=	bulk modulus
α_T	=	thermal expansion coefficient	$\boldsymbol{K}$	=	$k\alpha_T$ "diagonal tensor"
$\boldsymbol{D^*}$	=	effective stiffness tensor after "partial recovery"	C	=	damaged heat capacity
$\boldsymbol{K^*}$	=	effective diagonal tensor after "partial recovery"	A	=	TM damage parameter
C^*	=	effective heat capacity after "partial recovery"	η	=	degree of maximum stiffness recovery
$\boldsymbol{P_i}$	=	4th order project tensor for the projection in crack planes normal to direction i	$\boldsymbol{\delta}$	=	second order identity tensor

The space average of the density of net damage ($\bar{u}(t)$) is given in Table 1. The diffusion coefficient D_c depends on both pressure and temperature, following the constitutive model proposed in [9]. It requires more activation energy for a chloride ion to jump into a chloride vacancy than for a sodium ion to jump into a sodium ion vacancy [10]. So it can be reasonably assumed that migration of sodium ion dominates the diffusion of sodium chloride. According to Mapother's study [10] (temperature range: 573K ~ 973K), a linear relation between diffusion coefficient and temperature can be obtained in a log-scale plot:

$$D_c = -\frac{1.67\times10^{-12}}{T} + 2.99\times10^{-15} \qquad (9)$$

In which T is expressed in Kelvin, D_c is in m^2/s.

3.3. Upscaling Method

Grain rearrangement represents crack opening and closure, and grain cementation corresponds to rebonding. Microscopic cracks are assumed to be oblate spheroids, oriented perpendicular to the loading axis, as shown in Fig. 4. The link between fabric changes and phenomenological variables is established as follows:

- During elastic loading or unloading, only crack aperture varies
- When damage occurs, the crack length increases.
- Healing only occurs when the deformation in the loading direction is compressive. During healing, the crack length decreases whereas the aperture remains constant.

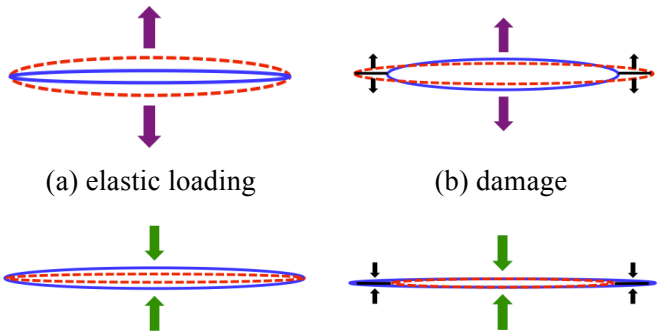

(a) elastic loading (b) damage

(c) elastic unloading (d) healing

Fig. 4. Geometric evolution of microcrack in the proposed model

The concept of crack density tensor [11] is adopted to account for the difference of crack length in the three directions of space. Assuming that the principal directions of stress and net damage are parallel, net damage eigenvalues ($\boldsymbol{A}$) are related to the means of the crack length components (R_j) as presented in Table 2. Standard deviation is considered constant, since sensitivity analyses showed that it does not vary significantly under the pressure and temperature conditions of the creep tests presented. Only the means m_i are updated, following the same approach as in [12]. So the probability density function of R_j can be updated from the macroscopic strain as:

$$\Delta\varepsilon \overset{Table\ 1}{\rightrightarrows} \Delta\boldsymbol{A} \overset{Table\ 2}{\rightrightarrows} \boldsymbol{R} \overset{Table\ 2}{\rightrightarrows} p_j(R_j) \tag{10}$$

Grains are considered as incompressible, so that the volume change of the REV is equal to the porosity change. The variation of three-dimensional void volume cannot be captured by microscopic observation. Therefore, a linear interpolation is used to correlate 3D porosity with 2D porosity. Given the lower and upper bounds of 2D and 3D porosities, the probability density function of void area can be updated:

$$\Delta\varepsilon \rightarrow \Delta n_{3D} \overset{Table\ 2}{\rightrightarrows} \Delta n_{2D} \overset{Table\ 2}{\rightrightarrows} p_A(A_v) \tag{11}$$

The lower bound of porosity is obtained at maximum packing. Salt grains tend to rearrange and form an ordered pattern. However, voids exist even at the maximum packing state since particles do not have perfect cubic shape. The lower bound of porosities is obtained by assuming that inter-granular voids are spheres (details are available in [13]). The upper bound of porosity is reached at the initial stage, when salt particles are assembled in loose packing before creep test starts. 2D porosities were obtained through microscopic observation. 3D porosities were approximated from experimental measures of sample deformation.

Using the strain decomposition, the stress tensor can be expressed as:

$$\boldsymbol{\sigma} = \boldsymbol{D}(\boldsymbol{\Omega}) : \boldsymbol{\varepsilon}^{\boldsymbol{E}} - \tau\boldsymbol{K}(\boldsymbol{\Omega}) \tag{12}$$

The stress rate under isothermal conditions writes:

$$\begin{aligned} d\boldsymbol{\sigma} &= \boldsymbol{D}(\boldsymbol{\Omega}) : d\boldsymbol{\varepsilon} + \frac{\partial \boldsymbol{D}(\boldsymbol{\Omega})}{\partial \boldsymbol{\Omega}} : \boldsymbol{\varepsilon} : d\boldsymbol{\Omega} - d\left[\boldsymbol{D}(\boldsymbol{\Omega}) : \boldsymbol{\varepsilon}^{\boldsymbol{id}}\right] \\ &= \boldsymbol{D}(\boldsymbol{\Omega}) : d\boldsymbol{\varepsilon} + \frac{\partial \boldsymbol{D}(\boldsymbol{\Omega})}{\partial \boldsymbol{\Omega}} : \boldsymbol{\varepsilon} : d\boldsymbol{\Omega} + d\boldsymbol{\sigma}_{\boldsymbol{R}} \end{aligned} \tag{13}$$

Micro-cracks are assumed to be non-interacting, so that the solid matrix surrounding each crack is considered as an isotropic linear elastic material. The theory of fracture mechanics [14] is used to compute the micro-crack opening vector of an ellipsoidal micro-crack propagating in mode I. The micro-crack displacement in the direction perpendicular to the micro-crack axis writes:

$$u_y(r,\theta) = \frac{K_I}{2\mu}\sqrt{\frac{r}{2\pi}}\sin\left(\frac{\theta}{2}\right)\left[\kappa + 1 - 2\cos^2\left(\frac{\theta}{2}\right)\right] \tag{14}$$

In which u_y is half of the crack aperture at location (r,θ), K_I is the stress intensity factor in mode I at the crack tip $(r = 0)$, and μ is the shear modulus of the linear elastic bulk material. κ depends on the bulk Poisson's ratio ν.

K_I depends on the microscopic residual stress that applies to the micro-crack faces: $K_I = \sigma_r\sqrt{\pi R}$. The half aperture $0.5\ \lambda_a$ defined above is equal to the displacement u_y when $\theta = \pi$, and $r = R$, in which R is half of the crack length:

$$\frac{1}{2}\lambda_a = \frac{\kappa + 1}{2\sqrt{2}\mu} R\sigma_r \tag{15}$$

With the void area $A_v = 0.5\pi\lambda_a R$, the macroscopic residual stress for N_v micro-cracks can be obtained (Table 2).

The probability density functions of fabric descriptors are updated with deformation and damage (Eq. (11) and (12)). Then the residual stress can be updated based on those descriptors (details are available in [13]).

The relations between fabric descriptors and macroscopic variables are summarized in Table 2. Figure 5 describes the computational method used to update macroscopic variables from the knowledge of microscopic descriptors.

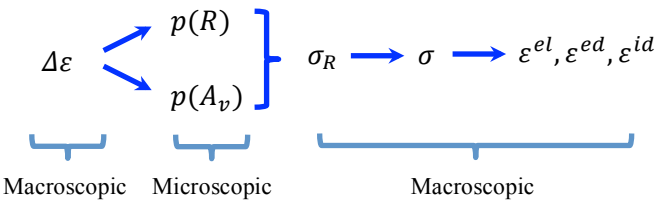

Fig. 5. Computation method to update macroscopic variables through the update of microscopic descriptors.

Table 2. Relations between microscopic and macroscopic variables.

Relation between fabric descriptor and phenomenological variables	
$\boldsymbol{R}$ and $\boldsymbol{A}$	$\boldsymbol{A} = \sum_{j=1}^{3} A_j e_j \otimes e_j$, $A_1 = N_v \frac{(\overline{R_2} \cdot \overline{R_3})^{3/2}}{V_{REV}}$, $A_2 = N_v \frac{(\overline{R_1} \cdot \overline{R_3})^{3/2}}{V_{REV}}$, $A_3 = N_v \frac{(\overline{R_1} \cdot \overline{R_2})^{3/2}}{V_{REV}}$ $\overline{R_j} = \int R_j p_j(R_j) dR_j$
n_{3D} and A_v	$\frac{n_{3D} - n_{3D,lower}}{n_{3D,upper} - n_{3D,lower}} = \frac{n_{2D} - n_{2D,lower}}{n_{2D,upper} - n_{2D,lower}}$ $n_{2D,lower} = \frac{A_{v,lower}}{A_{REV}} = \frac{\pi r^2}{l^2}$, $n_{3D,lower} = \frac{V_{v,lower}}{V_{REV}} = \frac{\frac{4}{3}\pi r^3}{l^3}$ $n_{2D,upper} = \frac{A_{v,upper}}{A_T}$, $n_{3D,upper} = \frac{V_{v,upper}}{V_T}$, $V_{v,upper} = V_T - V_s = A_{tube} \cdot L_{upper} - \frac{m_s}{\rho_s}$ $\overline{n_{2D}} = \int \frac{A_v}{A_{REV}} p_A(A_v) dA$
Relation between fabric descriptor and residual stress	
σ_R and R, A_v	$\sigma_R = N_v \sigma_r = N_v \frac{2\sqrt{2}}{\pi} \frac{\mu}{\kappa + 1} \frac{A_v}{R^2}$

$\overline{R_j}$	=	Mean value of crack length	A_j	=	Net damage in principal direction j
$n_{2D,lower}$	=	Lower bound of 2D porosity	V_{REV}	=	Volume of REV
$n_{3D,lower}$	=	Lower bound of 3D porosity	σ_R	=	Macroscopic residual stress for N_v cracks
$n_{2D,upper}$	=	Upper bound of 2D porosity	σ_r	=	Macroscopic residual stress for single crack
$n_{3D,upper}$	=	Upper bound of 3D porosity	A_T	=	Longitudinal cross-sectional area of the sample cylinder
V_s	=	Volume of the salt solid	V_T	=	Total volume of the sample cylinder
ρ_s	=	Density of the salt solid	A_v	=	Void area
m_s	=	Mass of the salt solid	A_{tube}	=	Inner cross-sectional area of tube

4. SIMULATION OF DAMAGE AND HEALING IN THE EXCAVATION DAMAGE ZONE

4.1. Problem Statement

Tunneling results in the formation of an Excavation Damaged Zone (EDZ) around the cavity. In salt rock, cracks can be rebonded under certain pressure and temperature conditions. A 2D problem of excavation followed by DMT-recovery was analyzed with the Finite Element Method (FEM). The simulations were performed in elasticity, for various levels of damage expected after excavation (from analytical stress distributions) and after recovery (from numerical predictions of healing at the material point). The tunnel was represented by a circular hole surrounded by an EDZ, itself embedded in intact rock (Fig. 6). The authors reckon that this preliminary study is not a true prediction of the EDZ, which would require the full implementation of the healing model in the FEM code. However, the analysis proposed is expected to give some insight on the potential benefits of rock healing on tunnel sustainability.

The far-field stress was kept unchanged throughout the simulation. In the first loading step, a hydrostatic pressure was applied at the wall of the tunnel, to simulate in situ stress conditions. In a second stage, stress at the wall was relaxed, to simulate the excavation. Before the excavation, all FE were assigned the same elastic properties (i.e. the EDZ material in the initial state is the same as the intact host rock). For given stress conditions and recovery times, rock stiffness in the EDZ was predicted at the material point, by assuming that stress elements in the EDZ are in pure tension. (a MATLAB program was used). Elastic moduli at various stages of the damage and healing process were then used as material parameters in the FEM code, in order to study the distribution of stress around the cavity at various stages of the recovery process. The approach adopted in the study is described in Figure 7.

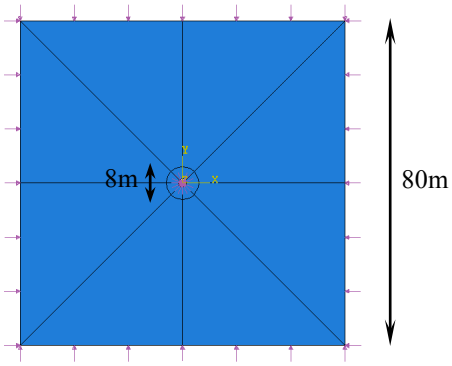

Fig. 6. Partition and boundary conditions adopted in the FEM model (cavity diameter = 2m).

4.2. Numerical Analysis at REV Scale

A strain-controlled test was programmed in MATLAB for the 1D stress path shown in Figure 7 (tension followed by closure, rebonding and reloading in tension). The REV porosity was entirely attributed to the micro-cracks, which makes the initial damage and the

initial residual stress non-zero. The probability density function of the void area was initialized from the initial porosity while the probability density function of the crack lengths was initialized from the initial volumetric damage. The solution of the diffusion equation averaged in space was approximated by truncating the infinite sum at N = 100.

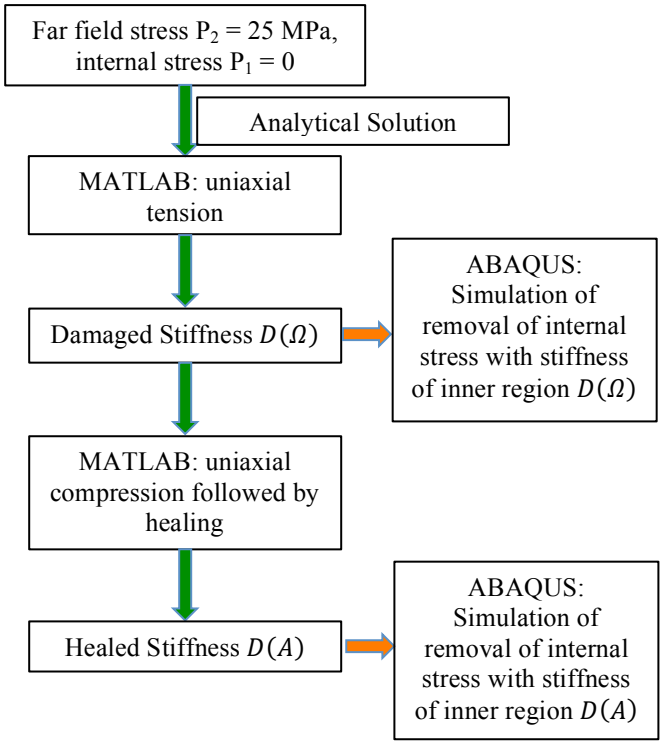

Fig. 7. Flow chart adopted for the numerical modeling.

The macroscopic damage and healing model depends on seven mechanical parameters and one thermal parameter. To the authors' best knowledge, relevant quantitative experimental data is absent for salt rock. For this preliminary study, a set of parameters fitted for sandstone was used, for illustrative purposes. The microscopic parameters were determined based on values found in the literature [15]. Model parameters are summarized in Table 3.

Table 3. Model parameters used for the strain-controlled uniaxial test (compression counted positive)

λ (Pa)	μ (Pa)	α (Pa)	β (Pa)
2.63e10	1.75e10	1.9e9	-2.04e10
g (Pa)	C_0 (Pa)	C_1 (Pa)	α_T (K^{-1})
1.1e8	200	1e5	-1e-5
U_0 (-)	l (m)	e_0 (-)	t (-)
1	1e-4	0.008	-1.2
$n_{2D,lower}$ (-)	$n_{2D,upper}$ (-)	$n_{3D,lower}$ (-)	$n_{3D,upper}$ (-)
0.03	0.165	0.004	0.321
R_{min} (m)	R_{max} (m)	A_{min} (m^2)	A_{max} (m^2)
1e-6	1e-5	1e-14	1e-12

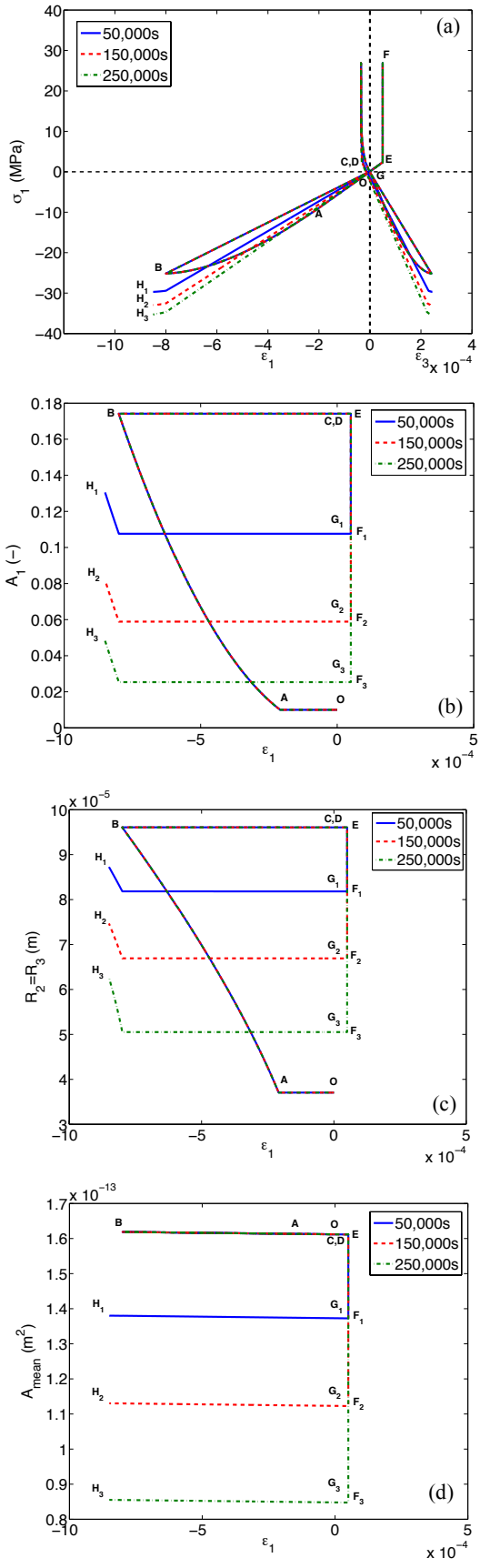

Fig. 8. Damage and healing simulated at the material point.

Numerical simulations were performed to study the effect of time on both macroscopic and microscopic variables. Mechanical loading and unloading phases

were carried out at room temperature (293K), whereas the healing process was simulated at elevated temperature (593K). Three different periods were imposed on the healing phases: 50000s, 150000s, and 250000s (about 3 days).

The stress-strain plots follow the expected trends (Fig. 8a). The response is elastic (OA) until damage initiates at point A. Cumulated damage degrades the stiffness before unloading starts (AB). After releasing all tensile stress (BC) and applying additional compression to close all cracks (CD), unilateral effects result in some recovery of the stiffness observed (DE). The increase of temperature results in healing (EF). Tensile deformation starts after decreasing the temperature and reloading (FG). Additional damage is produced after recovery (GH) when the new damage threshold is reached.

The evolution of net damage is similar in three simulations (Fig. 8b). Micro-cracks do not propagate during the elastic phase (OA) and unloading phase (BCDE). Damage increases during the non-elastic tension phase (AB), decreases during the healing phase (EF), and increase again during reloading (GH). During the creep process at constant axial deformation, h increases due to crack rebonding, causing decrease in A_1. Stiffness recovery is more important for longer healing periods. After 250,000s healing, the healed stiffness is getting close to its undamaged state.

Evolutions of fabric descriptors are presented in Figures 8c and 8d. Due to the axis-symmetry of the problem and by construction of the model, micro-cracks only propagate in planes orthogonal to the loading direction ($R_2 = R_3 \neq 0, R_1 = 0$). Since crack length is updated with net damage, evolution of crack length is similar to that of net damage.

The mean of void areas is proportional to the porosity of the sample, which is assumed to vary like the volumetric deformation. In the simulations, volumetric deformation mostly varies with axial deformation since it is about three times larger than lateral deformation. The mean void area decreases during healing phase as crack lengths shorten and crack apertures remain constant.

4.3. Preliminary FEM Analysis at Full Scale

Assuming that stress elements in the EDZ are in a state of pure radial tension, the elastic properties computed with MATLAB at different times after the excavation were used as input parameters in a FEM model designed with ABAQUS [16].

As an example, the spatial distribution of stress for t=250,000s is shown in Figure 9a. The stress distributions along the horizontal and vertical axis for a point at the top of the tunnel are plotted (σ_{rr} and $\sigma_{\theta\theta}$ in Fig. 9b). A discontinuity of stress is noted at the interface between the EDZ and the intact host rock, due to the difference of stiffness between the two zones. The transition zone is magnified in Figures 9c and 9d. After longer periods of time, healing reduces the stress discontinuity, which also indicates that the material can sustain higher stress in the EDZ. The distribution of stress gets closer to the undamaged stress distribution as healing progresses over time. It is worth noticing that both stress components (radial and orthoradial) are impacted by the damage and healing processes.

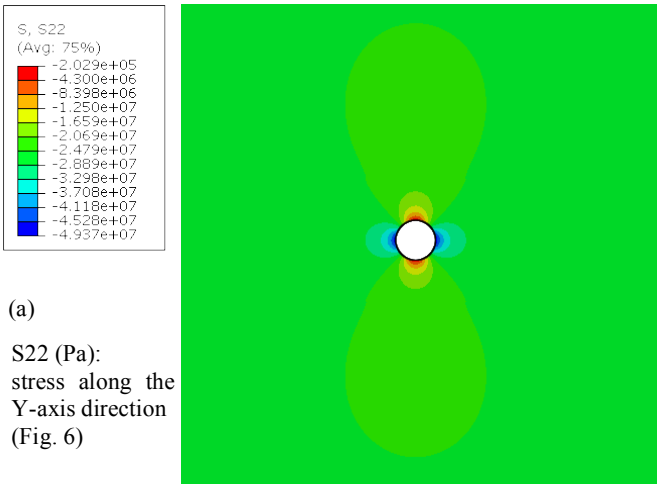

(a)

S22 (Pa): stress along the Y-axis direction (Fig. 6)

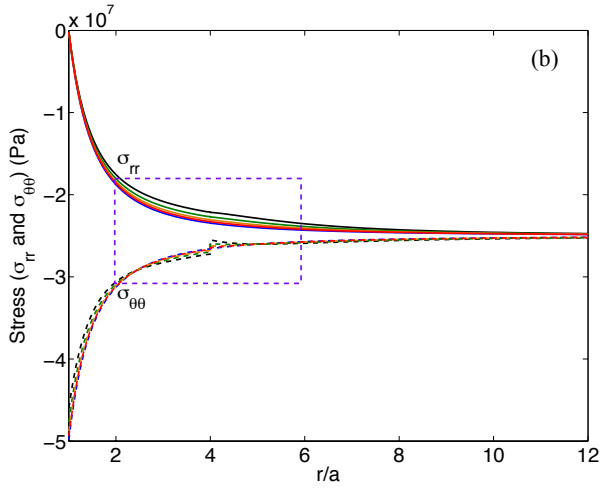

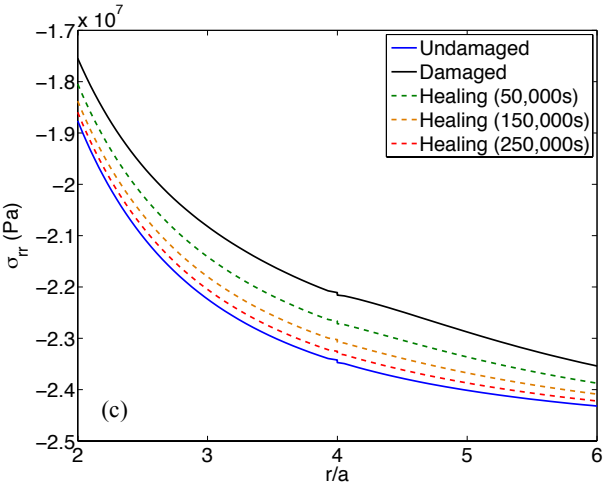

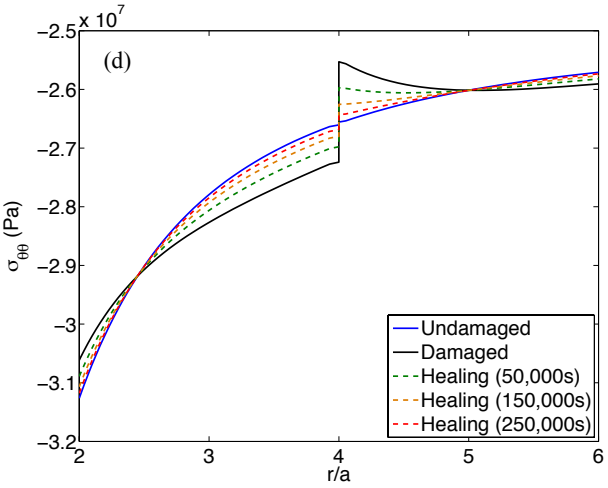

Fig. 9. Spatial distribution of stress around the cavity at different times after the excavation (a is the tunnel radius).

5. CONCLUSION

A model of damage and healing was developed within the framework of Continuum Damage Mechanics. It captures the anisotropy of stiffness and deformation induced by crack opening, closure and rebonding in salt rock. The free energy is postulated as a polynomial consisting of a purely thermo-elastic potential and a damaged energy component. The concept of unilateral effect is adapted to account for influence of crack closure on rock stiffness. Diffusive Mass Transfer is assumed to be the dominating mechanism for crack rebonding. Phenomenological variables are coupled to salt fabric descriptors: the void area and crack length are chosen to characterize the rearrangement and rebonding of the salt grains. This choice is supported by creep tests performed on table salt under constant stress and humidity conditions.

The constitutive model was programmed at the integration point in MATLAB to simulate thermo-mechanical loading and unloading cycles in axis-symmetric conditions. A stress path comprising a tensile loading, a compressive unloading, a creep-healing stage and a reloading was simulated for different healing periods. Analysis results follow the expected trends and satisfy the assumptions made in the framework. A preliminary Finite Element analysis was performed to study the distribution of stress around a cavity at different times after excavation. The simulations were performed in elasticity, with a prescribed damaged zone in which stress elements were assumed to be in pure tension. This allowed using the elastic properties predicted in MATLAB predictions as input parameters in the FEM analysis. A discontinuity of stress is noted between the damaged zone and the intact host rock. Damage and healing affect both the radial and hoop stress around the circular cavity. Healing tends to reduce the stress discontinuity over time, and overall the stress distribution evolves towards the elastic stress distribution.

The model highlights the impact of time on stiffness recovery and healing efficiency. In order to improve the predictions of stiffness, deformation and fabric, proper calibration with more experimental data is required. The proposed modeling approach is expected to improve the fundamental understanding of damage and healing in rocks at both macroscopic and microscopic scales, and to better predict the long-term behavior of geological storage facilities.

REFERENCES

1. Li, G. and N. Uppu. 2010. Shape memory polymer based self-healing syntactic foam: 3-D confined thermo-mechanical characterization. *Composites Science and Technology*. 70(9): 1419–1427.
2. Wexler, A. and S. Hasegawa. 1954. Relative humidity temperature relationships of some saturated salt solutions in the temperature range 0^0C to 50^0C. *Journal of Research of the National Bureau of Standards*. 53(1): 19-26.
3. Abramoff M.D., P.J. Magalhaes, and S.J. Ram. 2004. Image processing with ImageJ. *Biophotonics international*. 11(7): 36–42.
4. Zhu, C. and C. Arson. 2014. A thermo-mechanical damage model for rock stiffness during anisotropic crack opening and closure. *Acta Geotechnica*. DOI: 10.1007/s11, 440–013–0281–0.
5. Collins, I. and G. Houlsby. 1997. Application of thermomechanical principles to the modelling of geotechnical materials. *Proceedings of the Royal Society of London Series A: Mathematical, Physical and Engineering Sciences*. 453(1964): 1975–2001.
6. Dragon, A., D. Halm, and T. D´esoyer. 2000. Anisotropic damage in quasi-brittle solids: modelling, computational issues and applications. *Comput Methods Appl Mech Eng* 183(3): 331–352.
7. Chaboche, J.L. 1992. Damage induced anisotropy: on the difficulties associated with the active/passive unilateral condition. *Int. J. Damage. Mech*. 1(2): 148–171.
8. Arson, C., H. Xu, and F. Chester. 2012. On the definition of damage in time-dependent healing models for salt rock. Geotechnique Lett. 2(April-June): 67–71.
9. Weertman, J. 1955. Theory of steady-state creep based on dislocation climb. *Journal of Applied Physics*. 26(10): 1213–1217.
10. Mapother, D., H.N. Crooks, and R. Maurer. 1950. Self-diffusion of sodium in sodium chloride and sodium bromide. *The Journal of Chemical Physics*. 18:1231.
11. Kachanov, M. 1992. Effective elastic properties of cracked solids: critical review of some basic concepts.

Appl. Mech. Rev. 45(8): 304–335.

12. Arson, C. and J.M. Pereira. 2013. Influence of damage on pore size distribution and permeability of rocks. *International Journal for Numerical and Analytical Methods in Geomechanics.* 37: 810–831.

13. Zhu, C. and Arson, C. A model of damage and healing coupling halite thermo-mechanical behavior to microstructure evolution. *Geotechnical and Geological Engineering, Special Issue: Thermo-hydro-mechanical behavior of soils and energy geostructures* (under review).

14. Anderson, T. 2005. Fracture Mechanics: Fundamentals *and Applications.* 3rd Edition. Taylor & Francis.

15. Maleki, K. 2004. *Modélisation numérique du couplage entre l'endommagement et la perméabilité des roches – Application a l'é tude des ouvrages de stockage souterrain.* PhD Thesis, Ecole Nationale des Ponts et Chaussées.

16. ABAQUS/Standard User's Manual, version 6.9.